Chase-and-run dynamics in cell motility and the molecular rupture of interacting active elastic dimers

David Mayett,[1] Nicholas Bitten,[2] Moumita Das,[2,*] and J. M. Schwarz[1,†]
[1]*Department of Physics, Syracuse University, Syracuse, New York 13244, USA*
[2]*School of Physics and Astronomy, Rochester Institute of Technology, Rochester, New York 14623, USA*
(Received 29 December 2016; revised manuscript received 11 August 2017; published 11 September 2017)

Cell migration in morphogenesis and cancer metastasis typically involves interplay between different cell types. We construct and study a minimal, one-dimensional model composed of two different motile cells with each cell represented as an active elastic dimer. The interaction between the two cells via cadherins is modeled as a spring that can rupture beyond a threshold force as it undergoes dynamic loading from the interacting motile cells. We obtain a phase diagram consisting of chase-and-run dynamics and clumping dynamics as a function of the stiffness of the interaction spring and the threshold force and, therefore, posit that active rupture, or rupture via active forces, is a mechanosensitive means to regulate dynamics between cells. Since the parameters in the model differentiate between N- and E-cadherins, we make predictions for the interactions between a placodelike cell and a neural crestlike cell in a microchannel as well as discuss how our results inform chase-and-run dynamics found in a group of placode cells interacting with a group of neural crest cells. In particular, an argument was made in the latter case that the feedback between cadherins and cell-substrate interaction via integrins was necessary to obtain the chase-and-run behavior. Based on our two-cell results, we argue that this feedback accentuates, but is not necessary for, the chase-and-run behavior.

DOI: 10.1103/PhysRevE.96.032407

I. INTRODUCTION

During embryonic development as well as in cancer metastasis, cells often undergo migration in groups [1]. These groups are typically composed of cells of different types interacting with each other giving rise to nontrivial migration dynamics critical for their collective migration. For example, cocultures of stromal fibroblasts and carcinoma cells on top of an extracellular matrix (ECM) reveal that the carcinoma cells move within tracks in the ECM made by the fibroblasts [2]. Another example of a nontrivial migration mode occurs when embryonic cell populations of two different types, neural crest (NC) cells and placodal (PL) cells, are cultured next to each other on a polyacrylamide substrate [3]. NC cells are highly multipotent cells that migrate extensively during embryogenesis [4], while placodal cells (PL) remain more localized [3,5]. When cultured together, the NC cells chase the PL cells due to chemotaxis, while the PL cells run away from the NC cells. These examples suggest the following questions: What biochemical and/or biophysical mechanisms lead to different modes of migration resulting from the interplay of cells of different types? And how can such modes be modulated by cell-cell and cell-substrate interactions and possible feedback between them?

To begin to answer such questions via quantitative modeling with the NC-PL experiment in mind, we take a bottom-up approach and first characterize how two individual cells, each of a different type, move and interact in one dimension. While there are a number of models of single cell migration or even few cell migration of the same cell type [6–15], we will implement the active dimer model to describe each cell [16]. One of the strengths of the active dimer model is its simplicity making it an ideal candidate to generalize to two cells. Another strength of the active dimer model is that it connects experimentally known properties at molecular scales to mechanobiology at cellular scales.

In a nutshell, the active dimer consists of an active spring with focal adhesions acting as catch bonds at the leading cell edge and slip bonds at its rear [16]. The cellular activity is mechanosensitive and is incorporated as a changing equilibrium spring length depending on the loading state of myosin. Cellular motion arises as a result of the combined effect of cellular activity and the asymmetry in the mechanics of the focal adhesions at the front and the rear of the crawling cell. Using independently estimated parameters, individual cell speeds are in reasonable agreement with experimental observations for cells moving along ECM fibers, i.e., migration in one dimension [17]. Higher-dimensional generalizations of the active dimer model, while more complicated, are also possible. And yet, the chase-and-run (CAR) dynamics aforementioned could potentially be observed in one dimension, so one-dimension is the most natural place to make initial predictions.

To characterize the biophysical interaction between two cells, we will invoke a minimal set of assumptions based, in part, on experimental observations of single NC cells interacting with PL cells [3] and examine whether CAR dynamics emerge from the model or not. If CAR dynamics do emerge, how do the dynamics depend on parameter values and can these results be used to make testable predictions for one-dimensional motion? In addition to capturing the CAR phenomenon, we will ultimately be able to distinguish between various mechanisms for contact-inhibition-locomotion (CIL) in one-dimension—motion in which two cells move towards each other, collide, and then move away from each other [3,18–21].

Along the way we will also quantitatively test some of the qualitative ideas put forth in Ref. [3] to explain the CAR

*modsps@rit.edu
†jmschw02@syr.edu

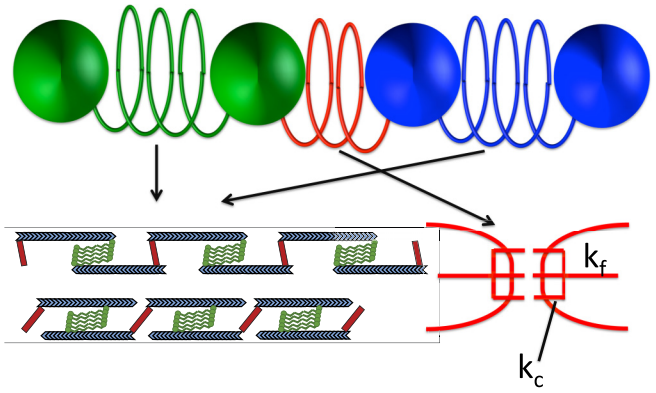

FIG. 1. Schematic representation of two cells (blue and green) with the red interaction spring containing N-cadherin molecules in parallel, each with spring stiffness k_c and a filopod with spring stiffness k_f. Each blue and green spring represents the prominent stress fibers along the length of the cell and, therefore, is active with both the extended mode (top) and contracted mode (bottom). The blue filaments represent actin filaments, red rectangles, α-actinin, and the green shapes, myosin minifilaments.

dynamics. Specifically, the authors argue both chemotaxis and CIL are necessary since if either the chemotaxis is blocked by genetically knocking down the cytokine implicated in NC chemoattraction in PL cells or genetically knocking down N-cadherins or inhibiting planar cell polarity (PCP) signaling, the CAR dynamics is no longer observed. Both N-cadherins and PCP signaling are thought to be responsible for CIL. This explanation can be tested at the two cell level. The authors argue that an important part of the CIL mechanism is that focal adhesions between the NC and PL cells are down-regulated. We can quantitatively test this idea by incorporating feedback between cell-cell interactions and cell-substrate interactions.

The paper is organized as follows. Section II contains a complete description of the model, Sec. III presents the analysis of the model, and Sec. IV summarizes the results and addresses implications.

II. MODEL

A. Single active elastic dimer

Cells moving along ECM fibers extend themselves and adhere to the fibers through focal adhesions, which are tractioned via contraction of longitudinal stress fibers; this migration mode is known as mesenchymal migration [17,22–25]. Pronounced stress fibers are a characteristic feature of this migration mode. Stress fibers primarily consist of actin filaments, myosin, and a passive cross-linker α-actinin [26]. Structurally, they can be thought of as made of parallel arrangements of actomyosin units in series, where each actomyosin unit may be considered as two actin filaments connected by a myosin mini-filament and the crosslinker α-actinin at each end (Fig. 1); i.e., each unit is a musclelike element [23,27].

These pronounced stress fibers in the mesenchymal migration mode are modeled as an active spring, or a spring with two different equilibrium lengths, x_{eq1} and $x_{\mathrm{eq1}} - x_{\mathrm{eq2}}$, corresponding to the unloaded and loaded states of myosin. Myosin exhibit catch bond behavior with an optimum load force of about 6 pN per motor. So myosin may not always be under sufficient load (or too much load) to walk efficiently along actin filaments [28]. Indeed, when new focal adhesions are just beginning to form at the front of the crawling cell, myosin are not pulling due to the small applied load. And when myosin are not pulling, the actin filaments extend to relieve the strain in the α-actinin and the mechanical stiffness of the active spring, k_1, is primarily due to the stiffness of the α-actinin. As the focal adhesions at the front of the cell mature over a time scale of seconds [29], the myosin are under enough load such that they "catch" and induce a contracted mode causing the α-actinin to stretch and rotate in the opposite direction. In this mode, myosin provide the mechanical stiffness of the spring and there is a second equilibrium spring length as indicated by the isolated stress fiber experiments [30]. As the myosin contract, strain builds in the α-actinin such that the myosin no longer "catch" due to too much load and a transition is then made to the extending mode.

Given these two modes of the stress fiber—passive extension and active contraction—the equilibrium spring length, x_{eq}, can be written as

$$x_{\mathrm{eq}} = x_{\mathrm{eq1}} - x_{\mathrm{eq2}}\Theta(x_1 - x_2 - l), \tag{1}$$

where $\Theta(x_1 - x_2 - l)$ is the Heaviside step function. The transition between the two modes is mechanosensitive. More precisely, it is determined by the extension of the spring: the larger the extension, the more the tensile load on myosin, thereby inducing contractility of myosin given its catch bond nature [28].

To account for potential conformational changes in the α-actinin, additional α-actinin binding in the contracted state due to the increasing overlap between actin filaments, as well as internal frictional losses, the equilibrium spring length takes on two different values depending on the history, i.e., $l^{\uparrow}$, as the active spring extends and $l^{\downarrow}$ as the active spring compresses with $l^{\uparrow} > l^{\downarrow}$. Therefore, the equilibrium active spring length takes on the form

$$x_{\mathrm{eq}} = x_{\mathrm{eq1}} - x_{\mathrm{eq2}}\Theta(x_1 - x_2 - l^{\uparrow}), \tag{2}$$

when the active spring is extending, and

$$x_{\mathrm{eq}} = x_{\mathrm{eq1}} - x_{\mathrm{eq2}}\Theta(x_1 - x_2 - l^{\downarrow}), \tag{3}$$

when the active spring is contracting. In other words, the description for x_{eq} contains *hysteresis*; see Fig. 2(a).

While the spring models the stress fibers of the cell, the beads denote the location of focal adhesions, which enable the stress fibers to connect to the ECM. Integrins are one of the main proteins comprising focal adhesions [31]. It has been shown that integrins can act as catch bonds under repeated loading [32]. We, therefore, conjecture that in the front of the cell, integrins are more likely to act as catch bonds due to the more dynamic environment of the maturation of focal adhesions. In the back of the cell, however, integrin act as typical slip bonds, where focal adhesions are merely being disassembled. Therefore, in the front of the cell, the initiation of focal adhesions call for a "small" friction coefficient, but once the focal adhesion forms and develops, it has a large friction coefficient when compared to an integrin slip bond. This "catching" mechanism of cell-track adhesion allows the cell's front to expand and explore new territory and after having

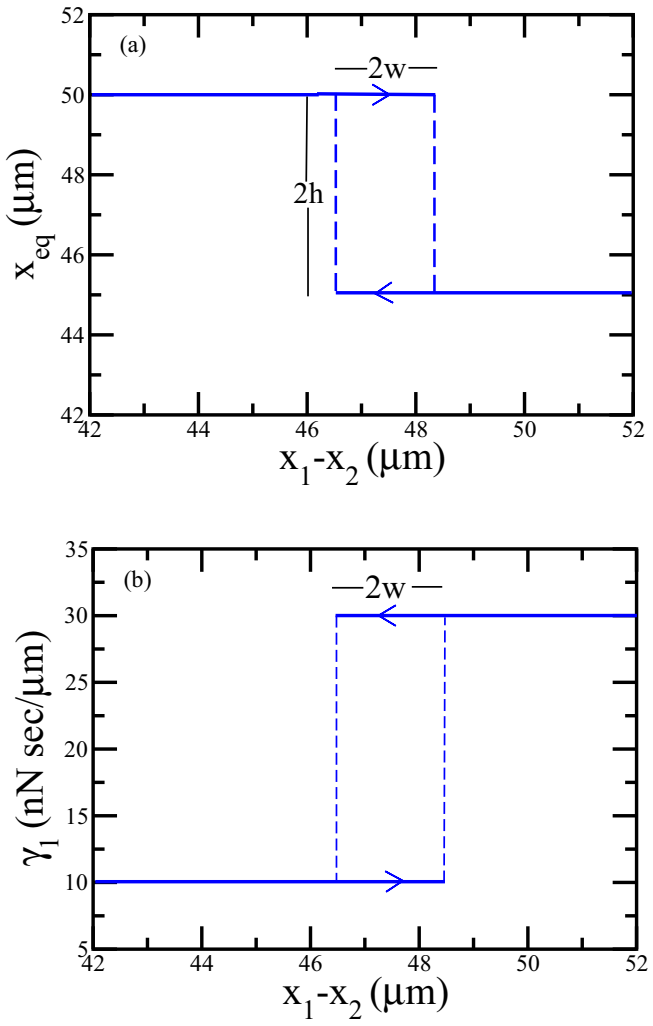

FIG. 2. (a) Plot of the equilibrium spring length of the active spring and (b) of the friction coefficient at the leading edge of the cell as a function of the active spring extension. From Ref. [16].

done that, then allows for the cell's rear to retract with the cell front not losing grip on the new territory it just explored due to the catch bond mechanism.

Since the stress fibers and the focal adhesions are connected (the stress fibers end at focal adhesions), we define

$$\gamma_1 = \gamma_{11} + \gamma_{12}\Theta(x_1 - x_2 - l^{\uparrow(\downarrow)}), \tag{4}$$

with $\gamma_{11},\gamma_{12} > 0$ and $\gamma_{11} < \gamma_{12}$. For small extensions of the cell, the friction at the leading bead is smaller than for large extensions. Larger friction implies a larger unbinding rate for integrins and, therefore, the integrins can more effectively grip the track. In addition, because the integrins track the myosin activity, the hysteresis exhibited by the myosin is also exhibited in the friction; see Fig. 2(b). Finally, γ_2, the friction coefficient for the now "rear" bead, is assumed to be constant with the integrins acting as ordinary slip bonds.

For the single active dimer case, the combination of activity that depends on the strain in the stress fiber and the asymmetry of the focal adhesions at the leading and rear edges leads to directed cell motion in the direction of larger friction [33]. To see this quantitatively, the active spring and focal adhesions are governed by the following active elastic dimer equation in the overdamped limit for the ith bead:

$$\gamma_i(x_1,x_2,l^{\uparrow},l^{\downarrow})\dot{x}_i(t) = \pm k_1(x_1 - x_2 - x_{\rm eq}(x_1,x_2,l^{\uparrow},l^{\downarrow})) + \sqrt{A_i}\zeta_i(t). \tag{5}$$

We have included an "active noise" term, where A_i is the variance of the active noise contribution due to stochasticity in motor activity, and $\zeta_i(t)$ is a Gaussian random variable with $\langle\zeta_i(t)\rangle = 0$ and $\langle\zeta_i(t)\zeta_j(t')\rangle = \delta_{ij}\delta(t-t')$. Here, A_i does not satisfy a fluctuation-dissipation relation and is not associated with any temperature.

One can transform to relative and center-of-mass coordinates using $x_s = x_1 - x_2$ and $x_{s,\rm cm} = \frac{x_1+x_2}{2}$, where the subscript s stands for single, to arrive at

$$\dot{x_s} = -\left(\frac{1}{\gamma_1(x_s,l^{\uparrow(\downarrow)})} + \frac{1}{\gamma_2}\right)k_1(x_s - x_{\rm eq}(x,l^{\uparrow(\downarrow)})),$$
$$v_{s,\rm cm}(t) = \dot{x}_{s,\rm cm} = -\left(\frac{1}{\gamma_1(x_s,l^{\uparrow(\downarrow)})} - \frac{1}{\gamma_2}\right)\frac{k_1(x_s - x_{\rm eq}(x,l^{\uparrow(\downarrow)}))}{2}, \tag{6}$$

depending on whether the spring is extending or compressing and in the limit of no active noise. A nonzero center of mass velocity translates to motion of the cell.

B. Two active elastic dimers

Now we consider two motile cells in one-dimension with each cell described by an active elastic dimer. To be concrete, the beads are described by their positions $x_i(t)$, with $i \in [1–4]$, where $i = 1$ denotes the rightmost bead and $i = 4$ the leftmost. The focal adhesions associated with the ith bead are denoted by γ_i. We set $\gamma_1 = \gamma_2$, which means the right cell is stationary given the symmetry in the friction, provided no outside forces act on it. This is our model PLL (placodelike) cell, since PL cells are less migratory than NC cells. More specifically, individual PL cells move about a third of the speed of NC cells on average [34]. By setting the velocity of the center of mass of the PLL cell in the absence of the NCL cell to zero, and then introducing the NCL cell—any nonzero velocity of the PLL cell center of mass will be due to the NCL cell. If the nonzero velocity averaged over a cycle is directed away from the NCL cell, then we will be observing the chase part of the dynamics. The model is particularly applicable to experiments studying one-dimensional cell migration in microchannels.

We now turn to the NC-PL cell population experiments [3] for further hints as to how to build a model determining the interaction between the two cells. The first observation is that the NC cells chemotact toward the PL cells excreting cytokine *Sdf1*, a known NC chemoattractant. The second observation from looking at the interface between NC and PL cells at the single cell scale is that the two different cell types form transient, but functional, cell-cell junctions. Data from the these transient, but functional, junctions indicates that the timescale for the collapse and destruction of the cell-cell junction is more abrupt than the timescale for the formation of the cell-cell junction. Both observations are just as relevant for the two-cell case as for the groups of two cells case. However, the group of PL cells in the experiments presumably

generate enough chemoattractant to drive chemotaxis. When examining collisions between individual NC-PL cells on a surface, the authors did not observe chase-and-run dynamics at the two-cell level [3]. The confinement of the two cells to a microchannel will concentrate the chemoattractant to enhance the possibility of chemotaxis of the NC cell toward the PL cell.

We now include these two, rather unambiguous, observations into the model with the above caveat of confinement triggering chemotaxis. As for our neural crestlike (NCL) cell (cell on the left), the action of chemotaxis is implicitly described by the breaking of the symmetry between the rear and front bead focal adhesion of the left cell to generate directed motion. Thus, for the cell on the left we have $\gamma_3 = \gamma_{33} + \gamma_{34}\Theta(x_3 - x_4 - l^{\uparrow(\downarrow)})$, and γ_4 is a constant. Both cells have changing equilibrium spring lengths denoted by $x_{\rm eq} = x_{\rm eq1} - x_{\rm eq2}\Theta(x_1 - x_2 - l^{\uparrow(\downarrow)})$ (for the PLL cell) to incorporate myosin driven contractility and α-actinin driven extensibility as described in Ref. [16].

To account for the transient, but functional, junction formation between the two cells, the cell-cell interaction, mediated by N-cadherin molecules localized at the ends of filopodia (actin-bundle-based protrusions) [35], is modeled as an interaction spring that forms when two cells come in close proximity (distance $\sim l_a$). Because the cells have their own inherent dynamics, they can pull on the cadherin bonds and rupture them [36]. It is this rupture phenomenon that may account for the difference in timescale between the formation of the cell-cell interface and the destruction of it [3]. The mechanical structure of the cell-cell junction will be assumed as follows: each cadherin molecule and the filopod are both linear springs of spring stiffness k_c and k_f, respectively. The cadherin springs are in parallel with each other followed by the filopod spring in series (Fig. 1). So the interaction spring elasticity is dominated the weaker spring, which is the filopodia spring since $k_f \approx k_c$ when comparing numbers [37,39] and $N_0 \gg 1$. We will use $k_f = k$ for notational ease. The interaction spring can rupture when $k_f(x_2 - x_3 - l_{\rm eq}) > N_0 f_c$, where N_0 is the number of cadherin molecules and f_c is the critical force threshold that will rupture an individual cadherin bond. Rupture can only occur when the two beads at either end of the interaction spring are moving away from each other. While rupture due to an applied force (static or dynamic) has been considered previously, we consider, for the first time in a model, rupture due to the interplay between active forces within each cell and intra- as well as intercellular mechanics.

Incorporating the different components of the model, the four coupled equations of motion of the beads are:

$$\begin{aligned}
\gamma_1(x_1,x_2,l^{\uparrow},l^{\downarrow})\dot{x}_1(t) &= -k_1[x_1 - x_2 - x_{\rm eq}(x_1,x_2,l^{\uparrow},l^{\downarrow})] \\
&\quad + \sqrt{A_1}\zeta_1(t) \\
\gamma_2(x_1,x_2,l^{\uparrow},l^{\downarrow})\dot{x}_2(t) &= k_1[x_1 - x_2 - x_{\rm eq}(x_1,x_2,l^{\uparrow},l^{\downarrow})] \\
&\quad - k[x_2 - x_3 - l_{\rm eq}] + \sqrt{A_2}\zeta_2(t) \\
\gamma_3(x_3,x_4,l^{\uparrow},l^{\downarrow})\dot{x}_3(t) &= -k_2[x_3 - x_4 - x_{\rm eq}(x_3,x_4,l^{\uparrow},l^{\downarrow})] \\
&\quad + k[x_2 - x_3 - l_{\rm eq}] + \sqrt{A_3}\zeta_3(t) \\
\gamma_4(x_3,x_4,l^{\uparrow},l^{\downarrow})\dot{x}_4(t) &= k_2[x_3 - x_4 - x_{\rm eq}(x_3,x_4,l^{\uparrow},l^{\downarrow})] \\
&\quad + \sqrt{A_4}\zeta_4(t).
\end{aligned}$$

TABLE I. Table of parameters used unless otherwise specified.

Parameters	Values
$k_1 = k_2$	1 nN/μm
$x_{\rm eq1}$	50 μm
$x_{\rm eq2}$	5 μm
$l^{\downarrow}$	46.5 μm
$l^{\uparrow}$	48.5 μm
γ_{11}	20 nN s/μm
γ_{12}	0 nN s/μm
γ_2	20 nN s/μm
γ_{33}	10 nN s/μm
γ_{34}	20 nN s/μm
γ_4	20 nN s/μm
N_0	100
l_a	0.5 μm
$l_{\rm eq}$	2 μm
A	0

For completeness, we have again included active fluctuations denoted by $\sqrt{A_i}\zeta_i(t)$, where $\zeta_i(t)$ is a Gaussian random variable with $\langle\zeta_i(t)\rangle = 0$ and $\langle\zeta_i(t)\zeta_j(t')\rangle = \delta_{ij}\delta(t - t')$. We will ultimately study the limit $A_1 = A_2 = A_3 = A_4 = A$. We have independent estimates for all but three parameters based either on experiments or prior modeling discussed in Ref. [16] or elsewhere. Please see Table I for the values of the parameters used unless otherwise specified.

For the interaction parameters, we know from single molecule experiments that $f_c = 40$ pN for N-cadherin and $f_c = 70$ pN for E-cadherin [38], $k = k_f$ is of order 1 nN/μm [39], and N_0 is of order 100 per pseudopod [40]. The only parameters we do not have independent estimates for are $l_{\rm eq}$, l_a, and A, though $l_{\rm eq}$ and l_a are determined by the appropriate lengthscales in the system. We set $l_a = 0.5$ μm and vary both $l_{\rm eq}$ and A.

To study this model, we implement fourth-order Runge-Kutta integration scheme in the absence of noise. With noise, we implement a Euler-Maruyama integration scheme. Both implementations use a time step of 0.005 s. We have checked our simulations against the analytical solution for some parameter values. For the single active dimer, there were two analytical solutions to be pieced together according to the cell's history. For the interacting active elastic dimer case there are eight analytical solutions to be pieced together according to each cell's history—two for each cell and two more cases for the interaction spring either on or off. Given the plurality of solutions, the majority of our results are based on simulations.

III. RESULTS

A. Single active dimer

Let us first briefly review the results for the dynamics of a single active dimer. Starting with Eq. (6), the solution for the relative coordinate as a function of time when the equilibrium spring length is $x_{\rm eq1}$ is

$$x_{s,I}(t) = x_{\rm eq1} + [x_s(0) - x_{\rm eq1}]e^{-\frac{k_1}{\gamma_2}\frac{(\gamma_{11}+\gamma_2)}{(\gamma_{11})}t}, \qquad (7)$$

and when the equilibrium spring length is $x_{\rm eq1} - x_{\rm eq2}$,

$$x_{s,II}(t) = x_{\rm eq1} - x_{\rm eq2} + [x_s(0) - x_{\rm eq1} + x_{\rm eq2}]e^{-\frac{k_1}{\gamma_2}\frac{(\gamma_{11}+\gamma_{12}+\gamma_2)}{(\gamma_{11}+\gamma_{12})}t}. \tag{8}$$

Depending on the history of the active spring, the solutions can be pieced together accordingly. For example, assume $x_s(0) \geqslant l^{\uparrow}$, then x_s decreases and obeys $x_{s,II}(t)$, which decreases exponentially with time. This is because the cell has "overextended itself" in its search for new territory and now the focal adhesions have matured so both the equilibrium spring length is decreased, due to myosin-induced contractility, and the front catch bonds "catch" such that the back of the cell can catch up with the front without losing new ground. After the initial decrease in x_s, as soon as x_s decreases below $l^{\downarrow}$, then the myosin effectively stop pulling, due to strain built up in the stress fibers from the focal adhesions and α-actinin, and the equilibrium spring length increases with new focal adhesions developing at the front. Once this happens, the time clock is "rezeroed" back to $t = 0$ and $x_{s,I}(t)$ is invoked, an exponential expansion given the initial condition, until x_s becomes larger than $l^{\uparrow}$ such that $x_{s,II}(t)$ solutions become valid once again and the process repeats itself.

This cyclic process in an overdamped system leads to net motion due to (1) the switching between the two equilibrium spring constants, which drives the overdamped system out-of-equilibrium, and (2) the asymmetry in the friction coefficients. Both properties are needed for motion. See $x_s(t)$, $x_{s,\rm cm}(t)$, and $v_{s,\rm cm}(t)$ in Fig. 3 for the parameters independently estimated in Ref [16]: $k_1 = 1$ nN/μm, $x_{\rm eq1} = 50$ μm, $x_{\rm eq2} = 5$ μm, $l^{\downarrow} = 46.5$ μm, $l^{\uparrow} = 48.5$ μm, $\gamma_{11} = 10$ nN s/μm, $\gamma_{12} = 20$ nN s/μm, and $\gamma_2 = 20$ nN s/μm. Using these independent estimates, one finds reasonable agreement with observed speeds of elongated cells crawling along ECM fibers [17]. The average speed of NC cells is approximately 0.03 μm/s [34], which average speeds in reasonable agreement with 0.033 μm/s for the single active elastic dimer using the above independent estimates.

As for the cyclic nature of the active dimer motility, the natural frequency of oscillation is given by $\omega = 2\pi/(t_I + t_{II})$ where $t_I = \beta \log \frac{h+w}{h-w}$ and $t_{II} = \alpha \log \frac{h+w}{h-w}$, respectively, where $\alpha = \gamma_2(\gamma_{11} + \gamma_{12})/k(\gamma_{11} + \gamma_{12} + \gamma_2)$, $\beta = \gamma_2\gamma_{11}/k(\gamma_{11} + \gamma_2)$, $w = \frac{1}{2}(l^{\uparrow} - l^{\downarrow})$, and $h = \frac{1}{2}x_{\rm eq2}$. Note that $w < h$ for motion to occur since the active strain energy generated by the myosin must overcome the strain barrier by the α-actinin.

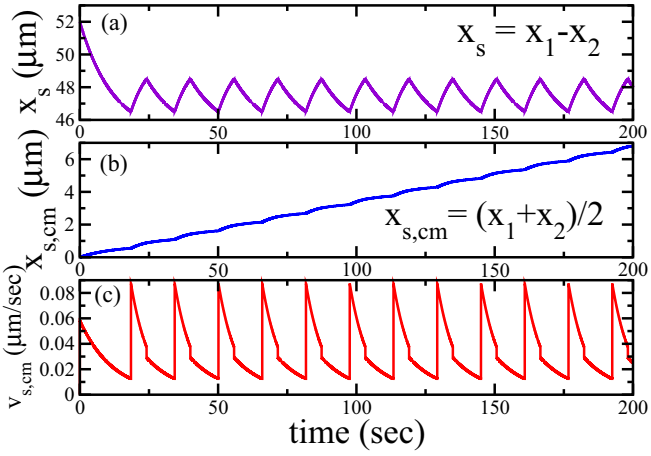

FIG. 3. (a) Plot of cell length $x_s = x_1 - x_2$ as a function of time for the parameters specified above for $k_1 = 1$ nN/μm, $x_{\rm eq1} = 50$ μm, $x_{\rm eq2} = 5$ μm, $l^{\downarrow} = 46.5$ μm, $l^{\uparrow} = 48.5$ μm, $\gamma_{11} = 10$ nN s/μm, $\gamma_{12} = 20$ nN s/μm, and $\gamma_2 = 20$ nN s/μm. (b) Plot of position of the center of mass, $x_{s,\rm cm}$, as a function of time for the same parameters. (c) Plot of the velocity of the center of mass as a function of time for the same parameters.

B. Two active dimers

To classify the types of interactions between the two different cells, we study the cell dynamics as a function of the junction spring stiffness, k, and the rupture force between cadherin molecules, f_r. We first focus on $x_{\rm rel} = x_2(t) - x_3(t)$, $x_{\rm cm,pl}(t) = \frac{1}{2}[x_1(t) + x_2(t)]$, and $x_{\rm cm,nc}(t) = \frac{1}{2}[x_3(t) + x_4(t)]$. We initialize the NCL cell some distance away from the PLL cell and iterate until they interact. As a result of the asymmetry in the friction coefficients of the NCL cell, it will migrate toward the PLL cell, mimicking the movement of the NCL cell toward the PLL cell due to chemotaxis. The PLL cell, on the other hand, does not move (on its own) since there is no asymmetry in its friction coefficients. Figures 4(a)–4(c) plot these quantities for $f_r = 0.01$ nN and $k = 5$ nN/μm as they interact. For these particular values, the cell springs are able to rupture the interaction spring, i.e., separate. While the two

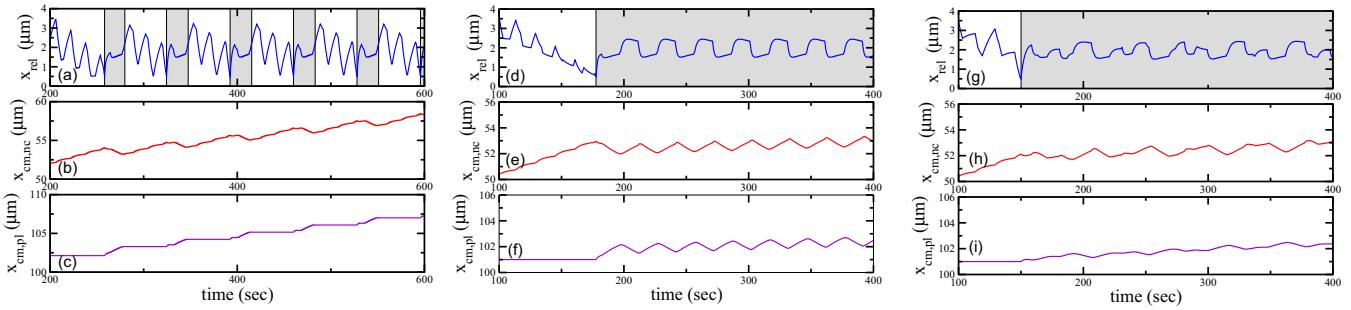

FIG. 4. (a–c) The relative distance between the two cells, the center of mass position of the neural crest, and the center of mass position of the placode cell, all as a function of time. Here, $f_r = 0.01$ nN and $k = 5$ nN/μm. The gray region in the top figure indicates when the interaction is tuned on. (d–f) The same as (a–c) but with $f_r = 0.03$ nN and $k = 5$ nN/μm. (g–i) Here, $f_r = 0.03$ nN and $k = 5$ nN/μm but with larger friction coefficients for the PLL cell. We have set the active noise strength $A = 0$ in these simulations.

cells interact, their separation first increases, then decreases, and immediately following rupture, the distance between the two cells is maximum. The rupture leads to a retraction of both cells away from each. But as the NCL cell, again, moves toward the PLL cell, the two cells interact again and the process repeats ad infinitum. We classify this dynamic state as *chase-and-run* behavior since the interaction spring is ruptured with the PLL cell pulling away from the NCL cell. Note that the position center of mass of the PLL cell only changes when in contact with the NCL cell.

Now we increase the rupture force to f_r to 0.03 nN; see Figs. 4(d)–4(f). At this increased rupture force for the cadherin molecules, the interaction spring remains on. In other words, the two cells do not separate once they interact, for the duration of the simulation for 20 min. We dub this dynamic state as *clumping*. This state is natural at higher rupture forces because there is not enough dynamic load between the two cells to actively break the cadherin springs. This statement then begs the question: is there a transition between CAR and clumping when the PLL cell is purely passive, or no activity? We find that there is no transition between the two types of dynamics when PLL cell is not active—only clumping occurs. So activity is necessary for the observing the CAR dynamics.

The clumping dynamics exhibits some interesting dynamics of its own. For example, if we increase the two friction coefficients of the PLL cell such that the time scales are different for each cell, for $f_r = 0.03$ nN and $k = 5\,\mathrm{nN}/\mu\mathrm{m}$, we observe quasiperiodic behavior in the relative distance between the cells; see Figs. 4(g)– 4(i). More specifically, as γ_{11} and γ_2 are varied between 35 nN s/μm to 45 nN s/μm, the solutions go from periodic to quasiperiodic back to periodic again. While more study of this quasiperiodic regime is presumably warranted from a mathematical standpoint, whether or not such quasiperiodicity can be observed experimentally, particularly in the presence of noise, is the more relevant issue at hand. In the absence of noise, we speculate that a ratio of incommensurateness emerges between the two natural frequencies of each active spring as mediated by the interaction spring for various regions of the clumped dynamics phase space.

One may also inquire about the velocity of the center of mass of the PLL cell as well as the velocity of the center of mass of the NCL cell in both the CAR phase and the clumping phase. The velocity of the center of mass of the NCL cell averaged over one cycle, $\bar{v}_{\mathrm{nc,cm}}$, is plotted in Fig. 5 for both phases. In steady state, $\bar{v}_{\mathrm{nc,cm}} = \bar{v}_{\mathrm{pl,cm}}$. The greater than zero average center of mass velocity (moving towards the right) for the PLL cell verifies the chase part of the CAR dynamics since the PLL cell would otherwise not move at all on its own by construction. With $\bar{v}_{\mathrm{pl,cm}} > 0$ in the clumping phase, the NCL cell is driving the PLL cell by breaking the symmetry between the two beads of the PLL cell and pushing it in the direction of the NCL cell. The averaged center of mass velocity is larger in the CAR phase in comparison to the clumping phase with the upper bound on $\bar{v}_{\mathrm{nc,cm}}$ being the single NCL cell value. A smaller rupture force promotes more rupture and it is the retraction of the PLL cell away from the NCL cell immediately following the rupture event driving the net displacement of the PLL cell. In the clumping phase, the average velocity of the center of mass of the NCL cell or PLL cell does not change

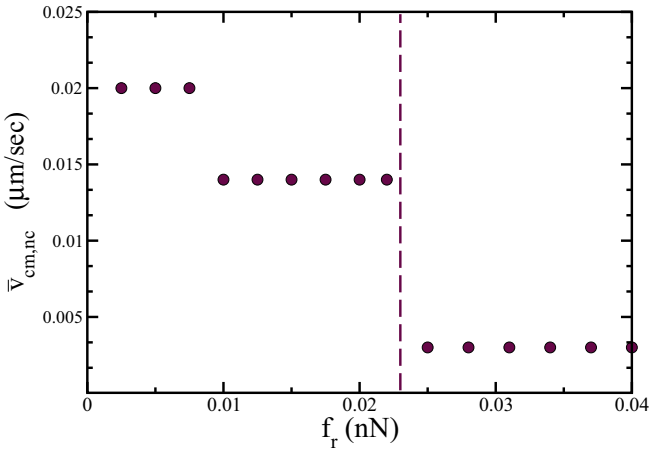

FIG. 5. The velocity of the center of mass for the NCL cell averaged over one cycle once the system has reached steady state as a function of rupture force with $k = 5\,\mathrm{nN}/\mu\mathrm{m}$. To the left of the vertical dashed line is CAR dynamics; to the right, clumping dynamics.

with rupture force since the interaction spring does not rupture. In the CAR phase, the two plateaus in $\bar{v}_{\mathrm{nc,cm}}$ as a function of f_r are due to the rectangular shape of the hysteresis in the equilibrium spring length of the two different active elastic dimers.

We also vary k, the spring constant of the interaction spring and determine its effect on the transition between CAR and clumping. For a small enough rupture force such that the system in the CAR phase, one can increase k to drive the system into the clumping phase. This because greater load is required to achieve the same strain making the system less likely to achieve the rupture threshold and so the two cell types remain bound. In addition, changing k does not affect much $\bar{v}_{\mathrm{cm,nc}}$. For instance, with $f_r = 0.02$ nN, $\bar{v}_{\mathrm{cm,nc}} = 0.015\,\mu$m/s for $k = 1\,\mathrm{nN}/\mu\mathrm{m}$; for $k = 10\,\mathrm{nN}/\mu\mathrm{m}$, $\bar{v}_{\mathrm{cm,nc}} = 0.013\,\mu$m/s.

In Fig. 6 we summarize our findings in terms of searching for CAR and clumping dynamics as a function of the interaction spring stiffness k and the rupture force f_r for an individual cadherin bond. Recall that the interaction spring connecting the two cells will rupture when the separation between them $x_2 - x_3$ exceeds $N_0 f_r/k + l_{\mathrm{eq}}$, where N_0 is the number of cadherin molecules and l_{eq} is the equilibrium length of a cadherin bond. This provides an analytical estimate for the phase boundary between the CAR and clumping dynamical states. For a fixed spring stiffness k, larger forces are required to disrupt clumped states than CAR states. Therefore, the system transitions from CAR dynamics at smaller rupture forces to clumping dynamics at larger rupture forces at fixed k. As the interaction spring stiffness increases beyond the cell spring stiffness, the energetics is dominated more by the interaction spring than the active loading by the cell springs and, hence, the dependence on the rupture force on the transition decreases. We can estimate the transition line by looking at the case where each cell spring is in its contracting phase (smaller equilibrium spring length) so that each cell spring maximally pulls on the interaction spring to potentially rupture it.

The deviation of the phase boundary obtained from the simulations from the analytical prediction can be explained as

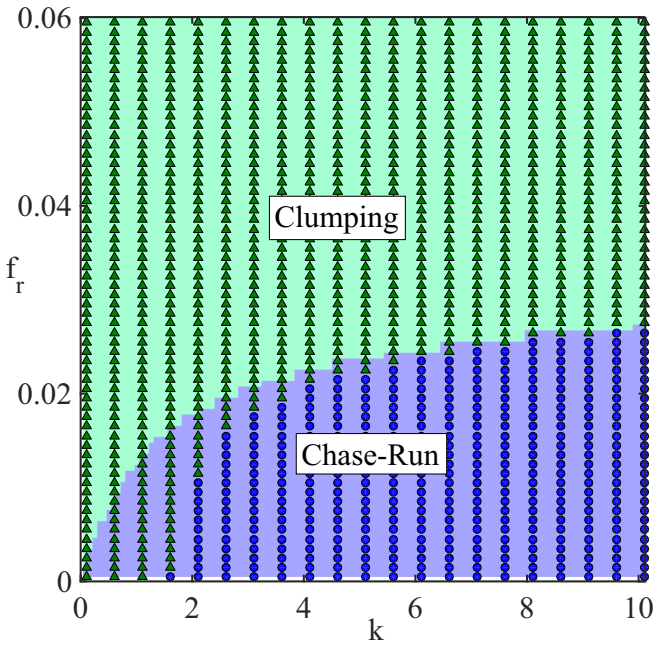

FIG. 6. Chase-run and clumping states for the two-cell model for the parameter values noted in the text. The symbols, blue circles (chase-run) and green triangles (clumping) indicate simulation data, while the corresponding blue and green shaded regions correspond to the analytical result. The units of k are nN/μm and the units of f_r are nN.

follows. To obtain the time series of the comigration of the two cells observed in the simulations, eight analytical solutions of coupled ODEs need to be pieced together—the active spring in each cell can be in a loaded or unloaded state, and the interaction spring between the cells can be on or off. Of these eight solutions, only one solution represents the comigration two interacting cells just preceding rupture. In obtaining the analytical estimate for the phase boundary in Figs. 6, 7, and 8, we focus on this solution. However, the solution will depend on the cells' history, thus giving slightly different values for

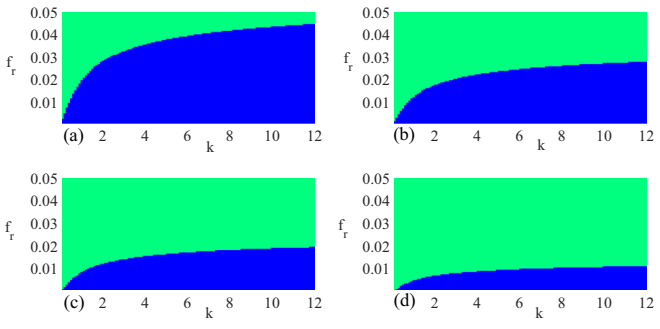

FIG. 7. Phase diagrams for the two-cell model as a function of h, with the chase-and-run state shown in blue (dark gray in grayscale) and clumped state shown in green (light gray in grayscale). Panels (a), (b), (c), and (d) correspond to $h = 7$, $h = 5$, $h = 4$, and $h = 3$, respectively. Parameter values used are the same as in the main manuscript except for x_{eq2}, which is changed to vary h. The units of k are nN/μm and the units of f_r are nN.

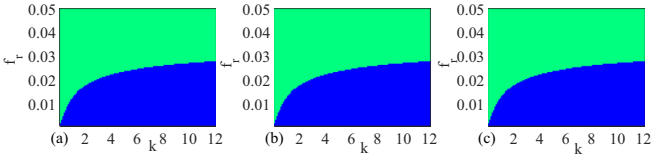

FIG. 8. Phase diagrams for the two-cell model as a function of w, with the chase-and run state shown in blue (dark gray in grayscale) and clumped state shown in green (light gray in grayscale). Panels (a), (b), and (c) correspond to $w = 2$, $w = 3$, and $w = 4$, respectively. Parameter values used are the same as in the main manuscript except for $l^{\uparrow}$ which is varied to vary w. Again, the units of k are nN/μm and the units of f_r are nN.

the analytical prediction and the result from the simulations in Fig. 6.

We further explore how the analytical estimates for the phase diagram depend on single cell parameters in Figs. 7 and 8. In addition to the dynamical phase, clumped or chase-and-run, depending on f_r and k, we expect it to also depend on how effectively the cells pull or contract to potentially rupture the cadherin bonds. This effectiveness is quantified by h, half the height of the hysteresis loop in the equilibrium length of the active cell spring shown the Fig. 2(a). The larger h is, the more the cell can contract and the greater the activity. Therefore, we expect the clumping region to shrink as h is increased. We indeed observe this behavior as shown in Fig. 7. On the other hand, varying w, half the width of the hysteresis loop in Fig. 2(a), does not alter the phase boundary; while w contributes to determining when the system is in the most contractile state, once there it doesn't impact whether the dynamics is CAR or Clumped (Fig. 8). The dependence of the phase diagram on h signifies that a theory of motility involving cell-cell interaction should depend on the mechanical properties of the cytoskeletal machinery in general, as expected, in addition to the rupture force of the individual cadherin molecules, which has not, to our knowledge, been explored before.

So far our results have been in the absence of noise and yet in biological systems there is active noise due to the presence of fluctuations in the myosin motors, for example. If our model is to have any relevance for biological systems, then we must explore whether or not the phase diagram we obtain is robust to active noise with $A > 0$. We find that most of the phase-diagram in Fig. 6 is robust to some range of the active fluctuation strength (see Fig. 9). How do we determine whether or not that range is physiologically relevant? For comparison, an estimate of variance of the thermal noise strength for each bead is $2\gamma k_B T = 2(20\,\text{nN s}/\mu\text{m})(4\,\text{pN nm}) = 1.6 \times 10^{-4}\,\text{nN}^2\,\text{s}$. Experiments on actomyosin networks demonstrate that the noise strength of the activity can be up to $\sim$10 times as strong as thermal noise [41], suggesting that the variance of the active noise could be as large as $10^{-3}\,\text{nN}^2\,\text{s}$. The values of A used in our simulations are thus well within the physiological range, with Fig. 9 indicating that our deterministic results are robust to active noise for k approximately greater than $5\,\text{nN}/\mu\text{m}$. However, for larger values of A, a system undergoing CAR dynamics in the absence of noise can be driven to clumping with large enough

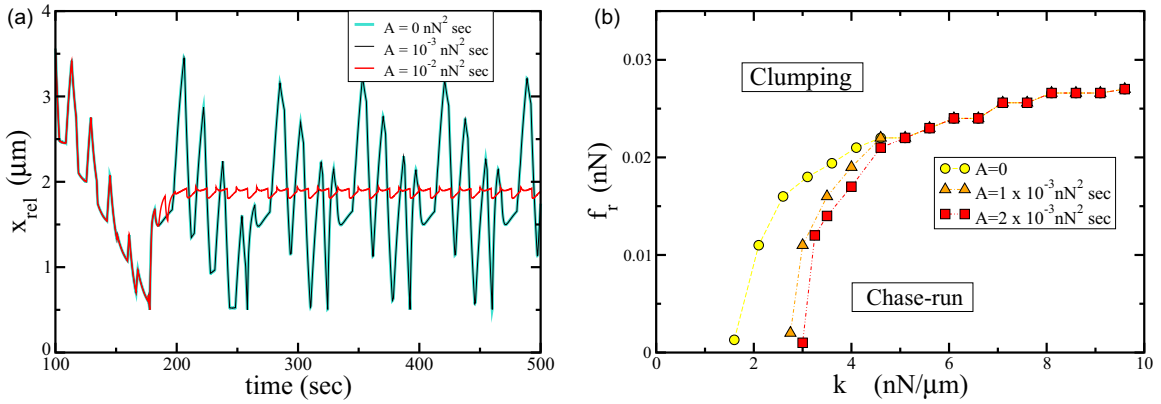

FIG. 9. (a) The relative distance between the cells with and without noise with variance A on each of the four beads. The curves with noise are typical curves. (b) The CAR-clumping phase boundary in the presence of noise, computed from the stochastic differential equation simulations.

fluctuations as indicated in Fig. 9(a). In summary, the CAR dynamics is robust for some range of A and k. We have here assumed uncorrelated, or Gaussian noise, for simplicity. Should active noise be an important contribution, we anticipate fluctuations that correlate with motor activity, so that correlated noise may be a more accurate representation of the system. Therefore, we leave further study of a more intricate form of noise, and how it affects the phase diagram, for a later date.

IV. DISCUSSION

We have constructed and studied a one-dimensional motility model of two different but interacting cells. The construction of the model was based on three assumptions: (1) that motile cells in one-dimension can be described as active elastic dimers, one with a nonzero center of mass velocity (NCL cell) and another with zero center of mass velocity (PLL cell), (2) that the NCL cell chemotacts to, or moves toward, the PLL cell, and (3) the cadherins form functional junctions between the two cells that can also rupture. The latter two assumptions are based on experiments of two different cell populations moving and interacting in two dimensions. Both assumptions should hold at the one-dimensional, two-cell-type level.

With the above minimal assumptions, we find both CAR and clumping dynamics. In the CAR phase, the NCL cell migrates toward the PLL cell, a functional cadherin junction between the two cells form. The junction then ruptures due to the active loading of the two cells and the two cells retract from each other. The NCL starts to, again, move toward the PLL cell. This transient interaction induces net motion in the PLL cell, which does not experience any net motion on its own. Both cells need to be active to observe CAR. As the rupture force threshold increases, we observe a clumping phase in which functional cadherin junction does not rupture and the two cells remain attached. There is net motion of the two-cell system in this phase as well, only the average speed is smaller than in the CAR phase. The clumping phase may be a generalization of trains of a single cell type observed in microchannels in which cells move collectively in one direction. In our model, however, the motion is driven by the NCL cell—the caboose of the two-cell train [19]. It is also reminiscent of chaining found in models of cells moving in microchannels [12].

Most of the CAR-clumping phase diagram is robust to physiologically relevant amounts of active noise so that it may indeed be a useful predictor for experiments of a NC cell and PL cell moving in a microchannel the size of a cell. Assuming that the chemoattractant of one slower PL cell is concentrated enough in the microchannel to coerce the NC cell toward it, we expect to observe CAR dynamics. If one could promote E-cadherin expression in the NC cell once the junction has formed, then one may observe clumping dynamics. Interestingly, as mentioned earlier, the rupture force for N-cadherin is approximately 40 pN, while for E-cadherin, it is approximately 70 pN. We observe, for example, for $k = 2\,\mathrm{nN}/\mu\mathrm{m}$, the doubling of rupture from 10 to 20 pN drives the system from CAR to clumping. The authors of Ref. [3] conjectured that the switching of N- to E-cadherin binding drove the NC cell and PL cell populations away from the CAR dynamics. We observe this in our two cell model as well within the appropriate force scale. Their conjecture is rooted in the observation that the switch from E- to N-cadherin promotes contact inhibition locomotion [42] and both chemotaxis and CIL is necessary for CAR. While detailed understanding of CIL is still lacking, our analysis brings to the table the potential importance of active rupture and how it, along with chemotaxis, predicts CAR in one-dimension from the biomechanics alone. Biochemistry can potentially either enhance or override the effect.

In the NC-PL cell population experiments, the experimentalists also conjectured that feedback between the cadherin and integrin is important for the CAR dynamics—the more cadherin bind, the less integrin bind [3]. We, however, observe CAR behavior even without any feedback between the two types of molecules at least at the level of two cells. We can, of course, incorporate this feedback into our model as follows. If the interaction spring is on, the friction coefficients on both sides of the spring are decreased, say, by half (in both states for the NC cell). With this feedback, we observe that the CAR state occupies a larger part of parameter space. For instance, with no feedback, the transition for $k = 5\,\mathrm{nM}/\mu\mathrm{m}$ occurs at $f_r = 0.021\,\mathrm{nN}$ but with the feedback, the transition occurs at $f_r = 0.023\,\mathrm{nN}$. Alternatively, a clumped system with no feedback can be driven to the CAR state with feedback; see Fig. 10(a). In any event, feedback between cadherins and

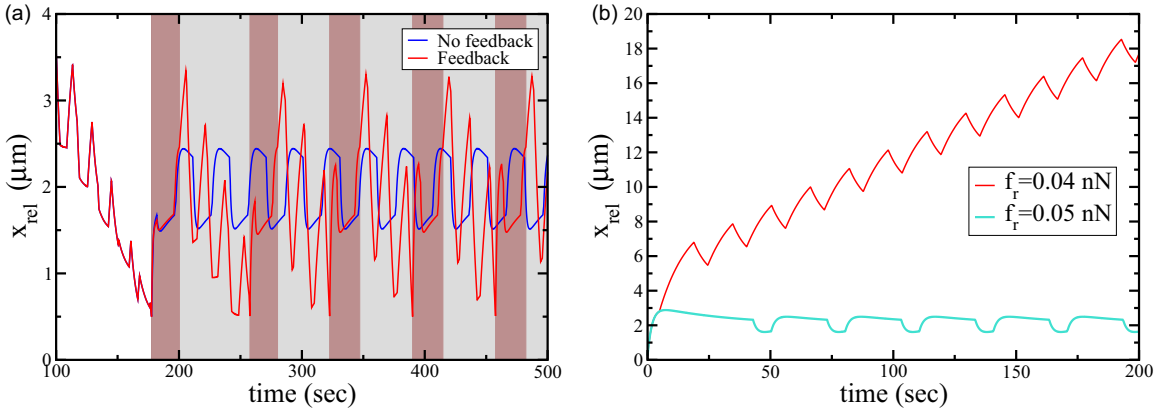

FIG. 10. (a) The relative distance between the two cells with and without feedback. The brown shading represents the presence of the interaction spring in the chase-and-run case, the gray, the clumping case. (b) Two cells moving apart from each other are not always able to rupture the interaction spring, i.e., escape. It depends on the rupture force. We have set the active noise strength $A = 0$ in these simulations.

integrins may be crucial for CAR in the experiments with populations of two cell types, but it is not at the two-cell level as in the model.

Furthermore, we conjecture that feedback between the cadherin and integrin binding could drive the cell to change its polarity and, therefore, potentially reverse direction. If the integrin binding becomes weaker on one side of the cell due to molecules participating more in the cadherin junctions than in the focal adhesions, then integrin binding on the other side of the cell may increase to compensate. This increase in ultimately friction on the other side of the cell may be enough to begin to generate motion away from the "other" cell. If the two cells rupture the interaction spring between them, which is not always the case in the modeling here, the two cells each go "their merry way." Rupture, therefore, may be an important part of the process. In Fig. 10(b), we show the relative separation between two cells moving away from each other for the cell-cell adhesion spring constant $k = 5\,\mathrm{nN}/\mu\mathrm{m}$ and other parameters as specified in Table I. We find that whether the connection between cells can be ruptured or not depends on the interplay between the intercellular interaction spring and the intracellular active cell springs. When the interaction spring does not allow the active cell springs to transition readily between the contracting and extending states, the cells cannot escape the other, resulting in clumped dynamics.

In addition to making predictions for the one-dimensional observation of CAR dynamics in a two-cell-type microchannel experiment, our model can be adapted to small groups of NCL and PLL cells. Each cell can be described as a collection of active springs with interaction springs between each cell. The interaction springs between the NCL and PLL cells would have a lower rupture threshold than the interaction springs between two PLL cells, for example. In this grouping of cells, one expects multiple junctions between the cells of two different types to form such that the rupture of multiple junctions becomes itself an interesting problem. Can the rupture of one junction trigger the rupture of nearby junctions, etc.?

Finally, our model connects molecular and cellular scales to provide a mechanistic understanding of collective migration of heterogeneous cells that combine mesenchymal migratory properties with cadherin-based cell-cell junctions. It may, therefore, not only apply to the enhanced migration of placode cells during morphogenesis, but also provide insights into micromechanical interactions between comigrating cancer cells and nontumorigenic cells, which are known to have significantly different mechanical and adhesion properties [43]. Our results suggest that a quantitative framework of coordinated cell migration and cell-cell interactions of more than two cells with varying degrees of motility should include molecular rupture forces [36] as well as the mechanosensitive activity of the cytoskeletal machinery.

ACKNOWLEDGMENTS

We acknowledge very helpful comments from one anonymous reviewer. D.M. and J.M.S. acknowledge support from NSF-DMR-1507938. N.B. and M.D. were supported by a Cottrell College Science Award from Research Corporation.

[1] P. Friedl, Y. Hegerfeldt, and M. Tusch, Collective cell migration in morphogenesis and cancer, Int. J. Dev. Biol. **48**, 441 (2004).

[2] C. Gaggioli *et al.*, Fibroblast-led collective invasion of carcinoma cells with differing roles for RhoGTPases in leading and following cells, Nat. Cell Biol. **9**, 1392 (2007).

[3] E. Theveneau *et al.*, Chase-and-run between adjacent cell populations promotes directional collective migration, Nat. Cell Biol. **15**, 763 (2013).

[4] E. Theveneau and R. Mayor, Neural crest delamination and migration: From epithelium-to-mesenchyme transition to collective cell migration, Dev. Biol. **366**, 34 (2012).

[5] G. Schlosser, Making senses development of vertebrate cranial placodes, Int. Rev. Cell Mol. Biol. **283**, 129 (2010).

[6] A. Mogilner, Mathematics of cell motility: Have we got its number? J. Math. Biol. **58**, 105 (2009).

[7] K. Keren, Z. Pincus, G. M. Allen, E. L. Barnhart, G. Marriott, A. Mogilner, and J. A. Theriot, Mechanism of shape determination in motile cells, Nature **453**, 475 (2008).
[8] E. L. Barnhart, G. M. Allen, F. Julicher, and J. A. Theriot, Bipedal locomotion in crawling cells, Biophys. J. **98**, 933 (2010).
[9] K. V. Kumar, S. Ramaswamy, and M. Rao, Active elastic dimers: Self-propulsion and current reversals on a featureless track, Phys. Rev. E **77**, 020102(R) (2008).
[10] A. J. Loosely and J. X. Tang, Stick-slip motion and elastic coupling in crawling cells, Phys. Rev. E **86**, 031908 (2012).
[11] E. Tjhung, A. Tiribocchi, D. Marenduzzo, and M. Cates, A minimal physical model captures the shapes of crawling cells, Nat. Comm. **6**, 5420 (2015).
[12] D. A. Kulawiak, B. A. Camley, and W.-J. Rappel, Modeling contact inhibition of locomotion of colliding cells migrating on micropatterned substrates, PLoS Comput. Biol. **12**, e1005239 (2016).
[13] B. A. Camley *et al.*, Polarity mechanisms such as contact inhibition of locomotion regulate persistent rotational motion of mammalian cells on micropatterns, Proc. Natl. Acad. Sci. USA **111**, 14770 (2014).
[14] F. J. Segerer, F. Thuroff, A. P. Alberola, E. Frey, and J. O. Radler, Emergence and Persistence of Collective Cell Migration on Small Circular Micropatterns, Phys. Rev. Lett. **114**, 228102 (2015).
[15] B. Li and S. X. Sun, Coherent motions in confluent cell monolayer sheets, Biophys. J. **107**, 1532 (2014).
[16] J. H. Lopez, M. Das, and J. M. Schwarz, Active elastic dimers: Cells crawling on a rigid track, Phys. Rev. E **90**, 032707 (2014).
[17] S. I. Fraley, Y. Feng, A. Giri, G. D. Longmore, and D. Wirtz, Dimensional and temporal controls of three-dimensional cell migration by zyxin and binding partners, Nat. Comm. **3**, 719 (2012).
[18] A. Pathak and S. Kumar, Transforming potential and matrix stiffness co-regulate confinement sensitivity of tumor cell migration, Integr. Biol. **5**, 1067 (2013).
[19] R. A. Desai, S. B. Gopal, S. Chen, and C. S. Chen, Contact inhibition of locomotion probabilities drive solitary versus collective cell migration, J. Roy. Soc. Interface **10**, 0717 (2013).
[20] M. Abercrombie and J. E. Heaysman, Observations on the social behavior of cells in tissue culture: I. Speed of movement of chick heart fibroblasts in relation to their mutual contacts, Exp. Cell Res. **5**, 111 (1953).
[21] C. Carmona-Fontaine *et al.*, Contact inhibition of locomotion in vivo controls neural crest directional migration, Nature **456**, 957 (2008).
[22] A. Roycroft and R. Mayor, Molecular basis of contact inhibition of locomotion, Cell Mol. Life Sci. **73**, 1119 (2016).
[23] P. Friedl, K. S. Zanker, and E. B. Brocker, Cell migration strategies in 3-D extracellular matrix: Differences in morphology, cell matrix interactions, and integrin function, Micro. Res. Tech. **43**, 369 (1998).
[24] A. D. Doyle, R. J. Petrie, M. Kutys, L. Matthew, and K. M. Yamada, Dimensions in cell migration, Curr. Opin. Cell Biol. **25**, 642 (2013).
[25] M. Mak, C. A. Reinhart-King, and D. Erickson, Microfabricated physical spatial gradients for investigating cell migration and invasion dynamics, PLoS ONE **6**, e20825 (2011).
[26] S. Tojkander, G. Gateva, and P. Lappalainen, Actin stress fibers: Assembly, dynamics and biological roles, J. Cell Sci. **125**, 1855 (2012).
[27] D. Mitrossilis, J. Fouchard, A. Guiroy, N. Desprat, N. Rodriguez, B. Fabry, and A. Asnacios, Single-cell response to stiffness exhibits muscle-like behavior, Proc. Natl. Acad. Sci. USA **106**, 18243 (2009).
[28] B. Guo and W. H. Guilford, Mechanics of actomyosin bonds in different nucleotide states are tuned to muscle contraction, Proc. Natl. Acad. Sci. USA **103**, 9844 (2006).
[29] Y. Chen, A. M. Pasapera, A. P. Koretsky, and C. M. Waterman, Orientation-specific responses to sustained uniaxial stretching in focal adhesion growth and turnover, Proc. Natl. Acad. Sci. USA **110**, 2352 (2013).
[30] K. Katoh *et al.*, Isolation and contraction of the stress fiber, Mol. Biol. Cell **9**, 1919 (1998).
[31] P. Kanchanawong, G. Shtengel, A. M. Pasapera, E. B. Ramko, M. W. Davidson, H. F. Hess, and C. M. Waterman, Nanoscale architecture of integrin-based cell adhesions, Nature **468**, 580 (2010).
[32] F. Kong, A. J. Garcia, A. P. Mould, M. J. Humphries, and C. Zhu, Demonstration of catch bonds between an integrin and its ligand, J. Cell Biol. **185**, 1275 (2009).
[33] M. Dembo and Y.-L. Wang, Stresses at the cell-to-substrate interface during locomotion of fibroblasts, Biophys. J. **76**, 2307 (1999).
[34] C. E. Shiau, R. M. Das, and K. G. Storey, An effective assay for high cellular resolution time-lapse imaging of sensory placode formation and morphogenesis, BMC Neurosci. **12**, 37 (2011).
[35] B. D. Hoffman and A. S. Yap, Towards a dynamic understanding of cadherin-based mechanobiology, Trends Cell Biol. **25**, 803 (2015).
[36] U. Seifert, Rupture of Multiple Parallel Molecular Bonds under Dynamic Loading, Phys. Rev. Lett. **84**, 2750 (2000).
[37] Z. Xu, D. Li, and B. Ji, Quantification of the stiffness and strength of cadherin ectodomain binding with different ions, Theoret. Appl. Mech. Lett. **4**, 034001 (2014).
[38] P. Panorchan *et al.*, Single-molecule analysis of cadherin-mediated cell-cell adhesion, J. Cell Sci. **119**, 66 (2006).
[39] T. Bornschlogl *et al.*, Filopodial retraction force is generated by cortical actin dynamics and controlled by reversible tethering at the tip, Proc. Natl. Acad. Sci. USA **110**, 18928 (2013).
[40] B.-A. T. Quang, M. Mani, O. Markova, T. Lecuit, and P.-F. Lenne, Principles of e-cadherin supremolecular organization in vivo, Curr. Biol. **23**, 2197 (2013).
[41] D. Mizuno, C. Tardin, C. F. Schmidt, and F. C. Mackintosh, Nonequilibrium mechanics of active cytoskeletal networks, Science **315**, 370 (2007).
[42] E. Scarpa, A. Szabo, A. Bibonne, E. Theveneau, M. Parsons, and R. Mayor, Cadherin switch during EMT in neural crest cells leads to contact inhibition of locomotion via repolarization of forces, Dev. Cell **34**, 421 (2015).
[43] W. Song, C. K. Tung, Y. C. Lu, Y. Pardo, M. Wu, M. Das, D. Kao, S. Chen, and M. Ma, Dynamic self-organization of microwell-aggregated cellular mixtures, Soft Matter **12**, 5739 (2016).